A 4E, Food, and Water Assessment and Machine Learning Optimization of a Novel Solar-driven Multigeneration System for Sustainable Production in Coastal California

Omid Malaie*,

Abstract

This study presents a novel machine learning-optimized multigeneration system to simultaneously address a coastal energy, water, and food production demands area. The proposed system combines photovoltaic-thermal, parabolic trough solar collectors, absorption refrigeration, organic Rankine cycle, multi-effect desalination, and hydrogen production via proton exchange membrane technology to maximize resource utilization. A comprehensive energy, exergy, economic, and environmental analysis is performed to evaluate the system's performance under various operating conditions. To overcome the computational burden of traditional optimization methods, a machine learning model is developed and validated to predict system performance, significantly reducing optimization time while maintaining accuracy. The neural network model is then employed to optimize key decision variables, considering multiple objective functions including energy efficiency, cost-effectiveness, and environmental impact. Key findings demonstrate that the optimized hybrid system achieves improved energy efficiency while supporting freshwater production and maintaining optimal greenhouse conditions. The results validate the system's potential to create a sustainable energy-water-food nexus, offering a viable solution for modern energy challenges. This research contributes to the field by presenting both a novel integrated system design and an innovative machine learning approach for rapid system optimization.

Nomenclature

Latin Symbols	A	Area	m²
	C	Concentration ratio	Dimensionless
	Cp	Specific heat capacity	J/kg·K
	D	Diameter	m
	i	Interest rate	%
	F	Faraday constant	C/mol
	G	Solar irradiance	kW/m²
	h	Specific enthalpy	kJ/kg
	J	Current density	A/m²
	k	Thermal conductivity	W/m·K
	L	Length	m
	m	Mass flow rate	kg/s
	N	Number of active hours per year	h
	n	Lifetime of the system	Years
	P	Power	kW
	Q	Heat transfer rate	kW
	T	Temperature	K
	u	Wind speed	m/s
	U	Overall heat transfer coefficient	W/m²·K
	V	Voltage	V
	w	Width	m
	W	Work	kW
	x	Quality	Dimensionless
	Z	Cost	$
Greek Symbols	α	Absorptance	Dimensionless
	β	Temperature coefficient	1/K
	γ	Reflectance of the mirror	Dimensionless
	η	Efficiency	Dimensionless
	κ	Thermal conductivity	W/m·K
	τ	Transmittance	Dimensionless
	ρ	Density	Kg/m³
	σ	Stefan-Boltzmann constant	W/m² ·K⁴
	ε	Emissivity	Dimensionless
	Φ	Maintenance and operation factor	Dimensionless
Subscripts	a	Ambient	
	act,	Activation overpotential	

a	(anode)	
act, c	Activation overpotential (cathode)	
b	Beam	
conv	Conversion	
ohm	Ohmic overpotential	
cond	Condenser	
ele	Electrolyzer	
eva	Evaporator	
gen	Generator	
in	Inlet	
inv	Inverter	
rad	radiation	
ref	Reference	
r	Receiver	
opt	Optical	
th	Thermal	
Abbreviations	ARC	Absorption Refrigeration Cycle
	COP	Coefficient of Performance
	CRF	Capital Recovery Factor
	FC	Fuel cell
	GH	Greenhouse
	HX	Heat exchanger
	LHV	Lower Heating Value
	ORC	Organic Rankine Cycle
	PTSC	Parabolic trough solar collector

1. Introduction

Growing awareness of fossil fuel's detrimental effects on the environment, climate, and public health has accelerated interest in renewable energy sources as alternatives [1]. Efficiently designed systems for heating, cooling, and power generation can further enhance domestic energy applications [2]. Integrating energy systems reduces costs while improving exergy efficiency or optimizing both simultaneously [3]. As renewable energy use expands, designing, analyzing, and optimizing co-generation systems has gained significant importance [4]. These systems involve multiple variables, making optimization critical for balancing environmental, economic, and energy considerations [5], [6].

Nafey et al. [7] examined solar organic Rankine cycle (ORC) integration with reverse osmosis desalination, assessing costs, energy, and efficiency. Results highlighted that solar collector fields significantly impact system efficiency and cost, with parabolic collectors emerging as the most economical choice. Ahmadi et al. [8] optimized combined-cycle power plants (CCPPs) for energy efficiency, cost rates, and CO_2 emissions. Exergy analysis revealed the combustor as the main site of exergy destruction, mitigated by raising gas turbine inlet temperatures and using efficient components. Nemati et al. [9] optimized a marine engine-based waste heat reverse osmosis (RO) desalination system linked with an ORC. Key findings indicated evaporator pressure significantly impacts system efficiency. The Pareto optimization approach identified a 37.4% efficiency and 59.106 USD/GJ as optimal. Kian Fard et al. [10] integrated reverse osmosis, a proton exchange membrane (PEM) electrolyzer, and a geothermal ORC. Their study attributed 59% of exergy destruction to the ORC and highlighted its dominant share of investment costs, with a repayment period of 5.6 years.

Behzadi et al. [11] optimized a solar-based cooling, electrical, and hydrogen production system. Systems with thermoelectric generators demonstrated superior exergy efficiencies and cost-effectiveness,

achieving a 12.01% efficiency and 0.1762 USD/hour cost rate. Niasar et al. [12] combined economic and exergy assessments in a multi-effect desalination system. Heat exchangers and expansion valves exhibited the highest and lowest efficiencies, respectively, with a repayment period of 5.844 years. Ghenai et al. [13] improved the performance of solar thermal multi-effect desalination by reducing specific energy consumption by 57.78% and enhancing freshwater production by 2.68 times via heat recovery techniques. Abdolalipouradl et al. [14] assessed geothermal-based tri-generation systems for electricity, hydrogen, and freshwater. Their double-flash ORC system outperformed the single-flash system in efficiency and economy. Askari and Ameri [15] evaluated multi-effect desalination systems integrated with solar energy. Freshwater costs varied by solar thermal technology, production rates, and seawater conditions, ranging from $2 to $3.

Bellos et al. [16] conducted a parametric study in 2020 using parabolic collectors integrated with absorption heat pumps and an organic Rankine cycle. Energy and exergy efficiency improved with higher generator temperatures. Increased generator heat input raised energy efficiency but reduced exergy efficiency. Solar radiation boosted electricity production but decreased both energy and exergy efficiencies. The system's consistent performance highlights its reliability and cost-effectiveness. In 2020, Khosravi et al. [17] used a multi-layer perceptron neural network optimized with an imperial competitive algorithm to model a geothermal-solar power system with absorption refrigeration. The model outperformed genetic algorithm-based methods in simulating system behavior. Solar radiation and water temperature differences increased power production. The system had an 8-year payback period at a 3% interest rate.

Alirahmi et al. [18] optimized a multi-generation system combining geothermal and solar energy to produce power, heat, cooling, hydrogen, and freshwater. The system achieved 28.95% energy efficiency and a unit cost of $129.7/GJ, highlighting its feasibility. Rostamzadeh et al. [19]

analyzed heat pump cycles in 2020 to enhance multi-effect desalination systems. Replacing traditional methods with multi-effect desalination systems-vapor compression heat pump (MED-VCHP) reduced energy loss from 145.4 kW to 129.6 kW and improved freshwater output, exergy efficiency, and specific work consumption. Rahmi et al.[20] evaluated a multi-objective energy system for Dezful city, integrating energy, exergy, and exergeoeconomic analysis. Results indicated a 31.66% energy efficiency and $21.9/GWh cost rate, with solar collectors and absorption chillers being the primary exergy destructors. Bozgeyik et al. [21] studied hydrogen production with PEM and ORC systems in 2020. ORC efficiency was 16.8%, while the overall system achieved 78% energy efficiency. Incorporating Multi-Stage Flash (MSF) desalination maintained hydrogen production while producing 5.74 m³/day of freshwater.

Sadat et al. [22] analyzed a solid oxide fuel cell multigeneration system, achieving 79.57% energy efficiency, 2771 kW heating capacity, and 1.4331 kg/h hydrogen production. The system showed excellent economic and energetic performance. Wegener et al. [23] examined biomass-based Combined Cooling, Heating, and Power (CCHP) systems, finding a 7% lifetime cost reduction and 75% greenhouse gas reduction. Optimal configurations depended on system size and climate conditions. Nami and Anwari [24] investigated small-scale CCHP systems using organic Rankine cycles. These systems achieved 63.6% efficiency and had a 4.738-year payback period, outperforming Rankine cycle-based systems.

Ren et al. [25] optimized solar-powered CCHP systems for different buildings. Results showed electric load strategies were most effective for office buildings, while wind-solar CCHP systems outperformed conventional setups. In 2021, Jiaxin Qian et al. [26] evaluated a wind-solar-CCHP system using contingency analysis and a multi-objective decision-making approach. The study demonstrated that wind-solar-CCHP systems outperform conventional CCHP systems by integrating

subjective and objective weights, improving evaluation accuracy. This method addresses limitations in existing evaluation techniques and supports the broader adoption of renewable energy systems in China. Chen et al. [27] evaluated Stirling engine-based CCHP systems for energy, cost, and CO_2 reduction. In Singapore, the system saved 75.9% energy and reduced CO_2 emissions by 70.1%. Deyin et al. [28] proposed a predictive control model for renewable CCHP systems. Optimization reduced costs by 16.92% compared to traditional load modes in hospitals.

A cost optimization model based on renewable energy sources and load forecasts was developed using interval optimization to match actual scenarios. The model uses feedback correction to adjust renewable energy sources and online data, reducing prediction errors and improving efficiency. The research, covering residential, school, and hospital areas, showed a 16.92% cost reduction in thermal load and 16.21% in electrical load. Ligai Kang et al. [29] assessed CCHP systems in various buildings, noting that while capital subsidies and feed tariffs influenced performance, residential use did not yield economic benefits. However, CCHP systems enhanced efficiency in hospitals and hotels. Ali Tawakkel Aghaei [30] proposed a CCHP system for the dairy industry with a gas turbine engine and backup boiler. Optimization methods aimed at high energy efficiency and cost reduction were evaluated. Sadeghi and Ahmadi [31] reviewed a CCHP system integrating compressed air energy storage (CAES) and CO_2 cooling. Their analysis showed high energy efficiency (68.19%) and reduced CO_2 emissions (157.09 kg CO_2/MWh). Finally, Xue et al. [32] examined a liquid air-based CCHP system, noting improved energy efficiency with an Organic Rankine Cycle for excess heat recovery.

In 2021, Prajapati et al. [33] reviewed the use of geothermal-solar groundwater desalination systems, highlighting their potential for future development. While solar and wind-powered desalination systems show promise, they are highly dependent on weather conditions. Geothermal energy offers a more reliable heat source, though its availability is

region-specific. In 2021, Safder et al. [34] combined a bagasse-biomass gasifier with a water unit to produce multiple energy sources. The study found that bagasse biomass flow rate significantly affected energy efficiency and cost. Optimizing the model improved energy efficiency by 43.07%, and energy production increased by 92.10%. Farsi et al. [35] assessed reverse osmosis desalination using a steam turbine in 2021, showing that combining multi-effect desalination with reverse osmosis significantly reduced costs and improved efficiency.

Ahmadi et al. [36] proposed an optimization model for a desalination system integrated with a gas turbine and cooling system, achieving cost savings and higher freshwater production. Behnam et al. [37] explored data-driven methods in desalination systems, noting their advantages for thermal and membrane-based technologies. Tahir et al. [38] reported advancements in multiple-effect distillation technologies, including the development of new antiscalants and vapor compression systems. Nasrabadi et al. [39] introduced a combined heat/cool load system with a gas turbine power plant for CO_2 capture, achieving up to 50% CO_2 emission reduction. They also analyzed power density parameters in a 2022 study, revealing that microchannel height significantly impacts performance. Mehrenjani et al. [40] conducted a comprehensive analysis of a renewable-based multigeneration system, finding that wind speed and solar collector area most affected the cost and energy efficiency. In another study, they designed a system for producing cooling, electricity, and hydrogen using geothermal energy, emphasizing the role of the heat exchanger in exergy destruction.

Despite numerous advancements in renewable energy-based systems and multigeneration frameworks, existing studies often focus on isolated technologies or lack an integrated approach to simultaneously meet electricity, water, and thermal demands. Furthermore, while some research incorporates solar energy into multigeneration systems, there is limited exploration of hybrid systems combining photovoltaic-thermal

collectors (PVT) and parabolic trough solar collectors (PTSC) to optimize energy and exergy efficiency.

This study addresses existing gaps by proposing a novel multigeneration system that integrates renewable energy technologies—such as photovoltaic-thermal (PVT) and parabolic trough solar collectors (PTSC)—with advanced thermodynamic cycles, including absorption refrigeration (ARC), Rankine cycle (RC), organic Rankine cycle (ORC), and multi-effect desalination (MED). Furthermore, the system incorporates hydrogen production via proton exchange membrane (PEM) technology and utilizes waste heat to support greenhouse operations, establishing a sustainable and efficient energy-water-food nexus. The system is meticulously modeled, analyzed, and optimized to maximize energy efficiency while minimizing environmental impact, demonstrating its potential as a viable solution to modern energy challenges. To overcome the computational limitations of traditional optimization methods, a neural network model is developed and trained to accurately predict system performance. Subsequently, a genetic algorithm is employed to optimize key decision variables, enabling efficient and cost-effective identification of optimal operating conditions. This approach not only enhances computational efficiency but also ensures the system's practical applicability in real-world scenarios.

2. System description

This study focuses on modeling, analyzing, and optimizing a novel multigeneration system. Solar collectors serve as the primary energy source for the system, which comprises several components: PVT, PTSC,

Figure 1: A schematic of the proposed system

ARC, RC, ORC, MED, PEM electrolyzer, and a greenhouse. The system operates as follows: In the PVT unit, part of the absorbed solar energy is converted into electricity, while the remaining energy is used to heat Therminol oil (Point 2). Some of this thermal energy is directed to the ARC system via a generator (Point 3). The Therminol oil is then reheated in the PTSC (Point 4) and subsequently transfers heat to the RC and ORC systems (Points 5 and 6, respectively). The electricity generated by the PVT, ORC, and RC systems is sent to the power management unit (PMU). From there, a portion is allocated for immediate consumption, while the surplus electricity is utilized by the electrolyzer to produce hydrogen. This hydrogen is stored for later use, enabling additional electricity generation during periods of high demand. The MED system is responsible for producing fresh water for the greenhouse (Point 29), utilizing heat from the ORC condenser (Point 25). The greenhouse receives the thermal energy it requires from the Therminol oil (Point 33), cooling from the ARC system (Point 31), and electricity from the PMU. A schematic representation of the proposed system is provided in Figure 1.

The Nipomo Dunes area is an ideal location for a solar power plant, offering ample open space, high solar irradiance, and proximity to the ocean and urban centers. Its favorable climate, especially during the hot season, ensures consistent and efficient solar energy production throughout the year.

3. Methodology

3.1. Energy Analysis

Energy balance equations are written as follows:

$$Q + \sum m_i (h_i - h_0) = W + \sum m_{out} (h_{out} - h_0) \qquad (1)$$

Electrolyzer and hydrogen storage systems

PEM electrolyzer systems use a proton-conducting membrane to split water into hydrogen and oxygen. They ensure high efficiency, quick response to variable power inputs, and ultra-pure hydrogen output, making them ideal for integration with renewable energy sources. The energy balances for fuel cells and electrolyzers are as follows [41]:

$$Power\,input = \frac{1}{\eta_{ele}} * m_{H2} * LHV_{H2}$$

(2)

$$Power\,output = \eta_{FC} * m_{H2} * LHV_{H2}$$

(3)

Water electrolysis requires the following amount of energy:

$$\Delta H = \Delta G + T \Delta S$$

(4)

In this equation, $T\Delta S$ and ΔG represent thermal energy and Gibbs free energy, respectively. According to this equation, hydrogen is produced at the following rate:

$$m_{H2,Produce} = \frac{J}{2F}$$

(5)

The Faraday constant is denoted by F, and J represents the density of the current. Hydrogen production requires the following amount of electricity:

$$E_{electrical}=J*V$$

(6)

$$V=V_0+\eta_{act,a}+\eta_{act,c}+\eta_{ohm}$$

(7)

$$V_0=1.229-8.5*10^{-4}(T_{PEM}-298)$$

(8)

where V_0 is the reversible potential of the electrolyzer, and V is the electrolyzer voltage. Additionally, the anode and cathode have respective activation overpotentials, while the electrolyte's ohmic overpotential is denoted separately.

Parabolic Trough Solar Collector

A PTSC system uses parabolic mirrors to concentrate sunlight onto a receiver tube, heating a working fluid like thermal oil. This heat is used to generate steam for electricity production. The energy output is calculated as follows [20]

$$Q_u=n_{cp}*n_{cs}*F_R\left[GA_a-A_rU_L(T_{ri}-T_0)\right]$$

(9)

where G can be written as:

$$G=G_b n_r$$

(10)

$$\eta_r=\gamma\tau_C\tau_P\alpha$$

(11)

$$F_R=\frac{m_cC_{p,c}}{A_rU_L}[1-\exp\left(\frac{-A_rU_LF_1}{m_cC_{p,c}}\right)]$$

(12)

$$F_1=\frac{1/U_L}{\frac{1}{U_L}+\frac{D_{o,r}}{h_{fi}}+(\frac{D_{o,r}}{2k}\ln\frac{D_{o,r}}{D_{i,r}})}$$

(13)

The surface of the aperture is:

$$A_a = (w - D_{o,r}) L$$

(14)

Photovoltaic thermal system

A PVT system combines photovoltaic and solar thermal technologies in a single unit, producing both electricity and thermal energy from sunlight. *Table 1* provides the correlation equations and relationships for the PVT simulation [4].

Table *1*: Correlation equations for PVT system

Energy principles	Input parameters
$P_{PVT} = Q_{PVT} \eta_{PV} \eta_{inv}$	$\eta_{opt} = 0.85, \eta_{inv} = 0.9, \eta_{Tref} = 0.12$
$Q_{conv} = hA(T_{gl} - T_a) + hA(T_{ins} - T_a)$	$h = 2.8 + 3 u_{wind}$
$Q_{th} = Q_{PVT}(1 - \eta_{PV})$	$T_{Sky} = 0.0552 * T_a^{1.5}$
$Q_{PVT} = GC\eta_{opt} A$	$\eta_{PV} = \eta_{Tref}[1 - \beta_{ref}(T_C - T_{ref})]$
$Q_{th} = Q_u + Q_{rad} + Q_{conv}$	$\beta = 0.004 K^{-1}, T_{ref} = T_0$
$Q_{rad} = \sigma\varepsilon A[(T_{gl}^4 - T_a^4) + (T_{ins}^4 - T_{sky}^4)]$	$u_{wind} = 2 \dfrac{m}{s}, T_a = T_0$

The concentration ratio C is denoted in Table 1 and G indicates the equivalent concentration of 1 kW/m2. Inverters receives heat from Q_{PVT}, which produces power. A further distinction between P_{PVT} and Q_{PVT} is that P_{PVT} represents the power output and Q_{PVT} represents the total absorbed heat of the PVT. Inverter efficiency and optimal efficiency are represented η_{inv} by η_{opt} and, respectively, while temperature coefficient β is the inverter's temperature coefficient.

The concentration ratio C is provided in Table 1, where G represents the equivalent solar irradiance of 1 kW/m². Heat from Q_{PVT} is transferred to inverters, generating power. P_{PVT} denotes the power output, while Q_{PVT} refers to the total absorbed heat of the PVT system. Inverter efficiency is represented by η_{inv}, optimal efficiency by η_{opt}, and the temperature coefficient of the inverter is denoted by β.

Organic Rankine Cycle

ORC systems efficiently generate power by converting low-temperature heat sourcesinto electricity using organic fluids with lower boiling points than water. The work produced by turbines is expressed as [39]:

$$W_T = m_{orc} * (h_{11} - h_{12})$$
(15)

The pumping work demand is calculated as:

$$W_P = \frac{m_{orc} * \Delta P}{\rho_f * \eta_{motor}}$$
(16)

The turbine isentropic efficiency is calculated as:

$$\eta_{is,T} = \frac{h_{11} - h_{12}}{h_{11} - h_{12,is}}$$
(17)

The net electricity production ORC cycle is calculated as:

$$P_{el} = \eta_g * \eta_m * (W¿¿ T - W_p)¿$$
(18)

The generator and shaft achieve 99% mechanical efficiency and 98% electrical efficiency. Heat input to the heat recovery system is calculated as:

$$Q_{hrs} = m_{orc} * (h_{11} - h_{14})$$
(19)

Multi-Effect Distillation

MED is an efficient thermal desalination process utilizing multiple stages to evaporate and condense seawater, reusing heat from previous stages

to minimize energy consumption. The heat transfer area for condensation and evaporation is determined using the following formulas [1]:

$$Q_e = U_e * A_e * \Delta T_i$$
(20)

$$Q_c = U_c * A_c * LMTD_e$$
(21)

A condenser's Logarithmic Mean Temperature Difference (LMTD) represents the effective temperature difference driving heat exchange. Heat evaporation begins at the end condenser and is calculated as follows:

$$U_e = 1.9695 + 1.2057 * 10^{-2} T - 8.5989 * 10^{-5} T^2 + 2.5651 * 10^{-7} T^3$$
(22)

$$U_c = 1.7194 + 3.2063 * 10^{-3} T + 1.5971 * 10^{-5} T^2 - 1.9918 * 10^{-7} T^3$$
(23)

Condenser and evaporator are represented by subscripts c and e, respectively.

The Gain Output Ratio (GOR) represents the amount of fresh water produced per unit of motive steam:

$$GOR = \frac{M_d}{M_m}$$
(24)

Absorption Refrigeration Cycle

ARC systems use thermal energy to drive the refrigeration process instead of mechanical work. The system employs an ammonia absorbent-refrigerant pair to generate cooling through heat exchange and absorption.

$$W_{pump} = m * (h_{20} - h_{19})$$

(25)

$$Q_{gen} = m_r * (h_{15}) + m_{ws} * (h¿¿22) - m_{ss} * (h¿¿21)¿¿$$

(26)

$$Q_{eva} = m_r * (h_{18} - h_{17})$$

(27)

$$COP = \frac{Q_{eva}}{(W_{pump} + Q_{gen})}$$

(28)

Condenser related energy equation:

$$Q_{cond} = m_8 * (h_{15} - h_{16})$$

(29)

Energy balance for the absorber is:

$$m_{18} h_{18} + m_{24} h_{24} = m_{19} h_{19}$$

(30)

The mass flow rate multiplied by specific exergy gives Ex. The following equation determines the heat loss or absorption by each component of the system:

$$m_{19} x_{19} = m_{18} x_{18} + m_{24} x_{24}$$

(31)

Also, for a pure refrigerant:

$$m_{19} x_{19} = m_{18} x_{18}$$

(32)

3.2. Exergy Analysis

Exergy analysis evaluates energy systems by assessing energy quality and work potential, highlighting inefficiencies through exergy destruction. It guides improvements in power generation, industrial processes, and renewables, enhancing system efficiency

Here are the equations for the exergy balance [39]:

$$\sum (1 - \frac{T0}{Tk}) Q_k - W + \sum m_i \, ex_i - \sum m_{out} \, ex_{out} = Ex_{dest}$$

(31)

Mass flow rate multiplied by specific exergy gives *Ex*. Following equations determine heat loss from or absorption by each component of the system:

$$Ex_L = Q_{\frac{L}{A}}(1 - \frac{T0}{T})$$

(32)

To determine the exergy lost or absorbed by the environment, Eq. 6 is used. As shown in *Table 2*, each system component has its own equation for exergy.

<div align="center">

Table 2: The components' exergy destruction

</div>

Component	Exergy destructing rates equations
ORC pump	$EX_{D,ORC,P} = EX_{13} + W_{ORC,P} - EX_{14}$
ORC condenser	$EX_{D,ORC,Cond} = EX_{25} + EX_{12} - EX_{26} - EX_{13}$
ORC turbine	$EX_{D,ORC,T} = EX_{11} - W_{ORC,T} - EX_{12}$
ORC heat exchanger	$EX_{D,ORC,HEX} = EX_{14} + EX_5 - EX_{11} - EX_6$
Greenhouse HEX	$EX_{D,GH,HEX} = EX_{32} - Q_{GH}(1 - T_0/T_s) + EX_{30} - EX$
Refrigerant expansion valve	$EX_{D,Refr,EXV} = EX_{16} - EX_{17}$

Solution expansion valve	$EX_{D,Solution,EXV} = EX_{23} - EX_{24}$
Solution pump	$EX_{D,SP} = W_{SP} + EX_{19} - EX_{20}$
ARC evaporator	$EX_{D,ARC,eva} = EX_{17} + EX_{30} - EX_{18} - EX_{31}$
ARC condenser	$EX_{D,ARC,cond} = EX_{35} + EX_{15} - EX_{36} - EX_{16}$
Absorber	$EX_{D,k} = EX_{18} + EX_{24} - EX_{19}$
PVT	$EX_{D,PVT} = EX_1 + Q_{PVT}(1 - T_0/T_s) - EX_2$
PTSC	$EX_{D,PTSC} = EX_3 + Q_{PTSC}(1 - T_0/T_s) - EX_4$

3.3. Economic Analysis

Exergoeconomy analysis combines exergy analysis with economic principles to evaluate the cost-effectiveness of energy systems. It assesses both thermodynamic performance and the economic impact of energy losses and resource use. By identifying the economic value of exergy destruction, exergoeconomy helps optimize system design and operation.

For the overall system, an effective interest rate of 4% and a 20-year lifetime are considered in the economic analysis. The cost index of each component can be calculated using the following relationship [14]:

$$Z_k = Z_k^{CI} + Z_k^{OM}$$

(33)

$$Z_k = \frac{Z_k * CRF * \Phi}{N}$$

(34)

In Table 3, the cost function for each component is shown as Z_k ($), where Z_k represents the cost of the k-th component. N denotes the number of active hours per year, Φ is the maintenance and operation factor, and CRF represents the capital recovery factor. The formula is as follows:

$$CRF = \frac{i(1+i)^n}{(1+i)^n - 1}$$

(35)

In this case, i represents the interest rate, and n indicates the lifecycle of the proposed system. From Eq. 34, the total cost rate is determined by evaluating all components. Fuel consumption costs are calculated using Eq. 36, and environmental cost rates, due to CO_2 emission penalties, are obtained from Eq. 37. Finally, the total cost rate is calculated by adding these three components together, as shown in Eq. 38:

$$C_f = C_f * m_{fuel} * 3600$$

(36)

$$C_{env} = C_{CO2} * m_{CO2} * 3600$$

(37)

$$C_{total,cost} = \sum_k Z_k + C_f + C_{env}$$

(38)

Table *3*: Components' capital cost functions [14]

Component	Cost Function

Heat exchanger	$Z_{HX} = 2143 * A_{HX}^{0.514}$
Absorption Chiller	$Z_{ARC} = 1144.3 * Q_{ave}^{0.67}$
ORC heat exchanger	$Z_{ORC,HX} = 2143 * A_{HX}^{0.514}$
ORC turbine	$Z_{ORC} = 4750 (W_T)^{0.75}$
ORC condenser	$Z_{ORC,con} = 516.62 (A_{Eva})^{0.6}$
ORC pump	$Z_{ORC,P} = 200 (W_P)^{0.65}$
Greenhouse	$Z_{greenhouse} = A_{greenhouse} * C_{greenhouse}$
Air blower	$Z_{AB} = 91562 * (\dfrac{W_{AB}}{455})^{0.67}$
Capital recovery factor	$CRF = \dfrac{i(1+i)^n}{(1+i)^n - 1}$
Lamp	$25 * N_{lamps}$

Input variables for economic analysis are listed in Table 4.

Table *4*: Input variables for economic analysis

Parameters	Values	Units
Φ	1.06	Dimensionless
i	12	%
C_{GH}	30	$/m^2
C_{fuel}	1	$/kg^3
C_{CO2}	0.024	$/kg
n	20	Years

$C_{GH,inc}$	107.639	$1/m^2$
N	7500	Hours

4. Results

The modeling is conducted using MATLAB CoolProp. Subsystems such as PVT, PTSC, MED, and PEM are validated with theoretical data. A comparison between the presented MED model and the data from [1] is shown in Table 5, demonstrating good agreement. To verify the PVT model, its parameters are compared with those from [4], as presented in Table 6, showing a decent match. Similarly, the PTSC system is validated by comparing thermal parameters with data from [20], with results indicating good agreement in Table 7. Furthermore, the PEM model is validated against [41], as illustrated in Figure 2.

Table 5: Verification of MED modelling with [1]

Parameter	Code	Reference
M_s	0.1729	0.1726
Pr	5.78	5.79
Q_c	389.98	389.44
A_c	32.68	32.62

Table 6: PVT system modelling validation with [4]

Parameter	Code	Reference
Q_{pv}	85000	85000
P_{pv}	635.5	634.9
Q_{th}	7786	7794.5

Table 7: Results of modelled PTSC compared to [20]

Parameter	Code	Reference
F_r	0.9	0.9
Q_u	22901	23028

T_o	273	273.3
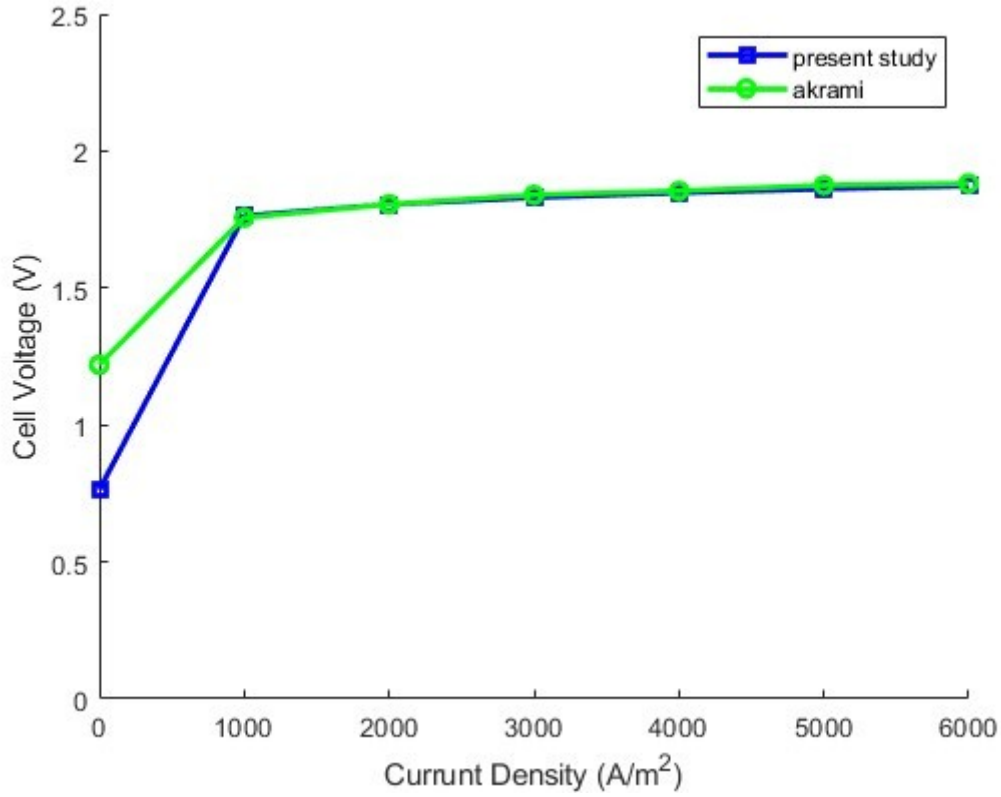
Figure 2: PEM modelling Comparison Between Present Study and [41]

4.1. Parameter Study

The analysis results for $T_{amb}=21 \circ C$ are presented in Table 8, which lists the thermal, exergy, and economic properties of each stream. In the parameter study, the effects of PVT area, greenhouse length, number of solar cells, number of MED stages, and T_1 on energy efficiency, exergy efficiency, GOR, and annual interest are evaluated. Each parameter is varied individually while the others remain constant.

Table 8: The System States

	Fluid	T(K)	P(Pa)	$\dot{m}$(kg/s)	h(j/kg)	Ex(W)	$\dot{C}(\$/h)$
1	Therminol-VP1	373.15	1000000	220	133611.3	3558960	3.56E+18
2	Therminol-VP1	428.5232	1000000	220	236179.5	9553918	3.56E+18
3	Therminol-VP1	424.4085	990000	220	228267.5	9012280	4.51E+18
4	Therminol-	653.671	980100	220	737648	595962	4.51E+

					.2	80	18
	VP1						
5	Therminol-VP1	413.15	980100	220	206874.2	7612145	5.76E+17
6	Therminol-VP1	309.7294	980100	220	26649.35	324166	2.45E+16
7	Water	643.671	4000000	43.01096	3143845	51046145	677.1278
8	Water	375.728	1111111.1	43.01096	2467456	20755257	677.1278
9	Water	375.4422	110000	43.01096	428838.7	6962357	-1.59E+19
10	Water	375.4525	4000000	43.01096	428949.4	1721737	-3.93E+18
11	R245fa	412.65	200000	117.5055	536275.5	3626513	1047700
12	R245fa	382.0796	50000	117.5055	506060.6	-228938	-66140.2
13	R245fa	271.5491	49500	117.5055	198723.2	606996	-5.40E+17
14	R245fa	271.6055	200000	117.5055	198849	619371.4	-5.51E+17
15	Ammonia	308.1301	1350000	1.812395	1488332	630670.6	6.31E+09
16	Ammonia	308.1301	1350000	1.812395	365975.6	-1403483	-1.4E+10
17	Ammonia	259.4982	250000	1.812395	365975.6	538379.2	5.38E+09
18	Ammonia	259.4982	250000	1.812395	1446112	2453098	2.45E+10
19	Ammonia	306.7788	250000	7.249579	44518.09	-1.1E+07	-9.7E+10
20	Ammonia	306.9168	1350000	7.249579	46038.65	-983998	-8.4E+09
21	Ammonia	367.5505	1350	7.249579	343460.6	1170601	9.94E+09
22	Ammonia	411.8886	1.35E+09	7.249579	527929.1	114399.8	-2.5E+10
23	Ammonia	266.323	1350000	7.249579	-114591	-4543604	-6.9E+09
24	Ammonia	266.579	250000	7.24957	-	-	-

4				9	114591	455623	6.9E+08
25	Water	373.15	101418	16.00503	2675570	42873384	2.14E+09
26	Water	373.15	101418	16.00503	419166.2	-2.8E+07	5.40E+17
27	Water	298.15	3169.929	782.5518	104829.2	-2.2E+08	5.40E+17
28	Water	313.15	7384.938	46.29823	167533	2903741	0
29	Water	340.1602	27380.79	30.86549	280536.7	3560923	860315.5
30	Water	284.4731	250000	100	48878.92	-2.2E+07	0
31	Water	289.15	250000	100	68455.25	143057.6	-1.9E+10
32	Water	0	0	0	0	0	-1.9E+10
33	Water	0	0	0	0	0	0
34	Water	294.15	111111.1	100	88200.19	980.5745	0
35	Water	375.4422	110000	100	965029.1	15603051	1.59E+19
36	Water	298.15	1350000	100	106075.8	136344.3	0
37	Water	303.0199	1350000	100	126417.4	179847.2	2.03E+10

The main results are comprehensively discussed and illustrated in Figs. 3–7. This research analyzes how variations in factors affect energy efficiency, exergy efficiency, GOR, and yearly interest, providing insights into both technical performance and financial implications. Figs. 3–7 visually depict these relationships, with each parameter's effect scaled for clarity. The study aims to understand the stability, sensitivity, and trade-offs between efficiency and financial metrics, guiding system design and operational strategies. By evaluating parameter-dependent patterns, it identifies areas to maximize efficiency without significant financial costs and highlights financial indicators sensitive to operational

changes. This research offers valuable insights into optimizing energy systems for technical and economic feasibility.
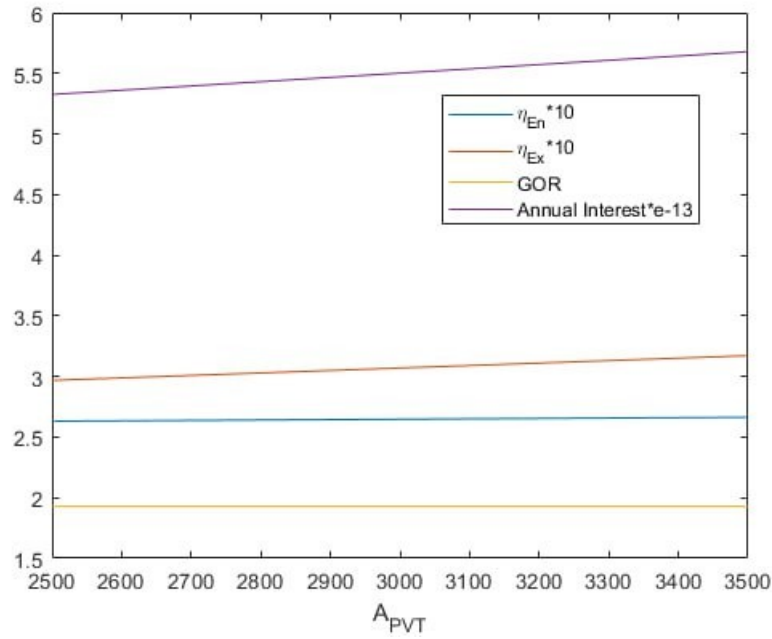
Figure 3: Relationship between A_PVT and key performance metrics: efficiency, GOR, and annual Interest

Figure 3 illustrates the relationship between A_{PVT} and four variables: η_{En}, η_{Ex}, GOR, and Annual Interest, each plotted on a distinct scale for clarity. The energy and exergy efficiencies, scaled by 10, exhibit minor increases or stability as A_{PVT} grows. GOR remains nearly constant, indicating stable production efficiency, while Annual Interest, scaled by e^{-13}, shows a more pronounced increase, highlighting its greater sensitivity to changes in A_{PVT}. Overall, the graph demonstrates that within this range, Annual Interest is the most responsive parameter to variations in A_{PVT}.
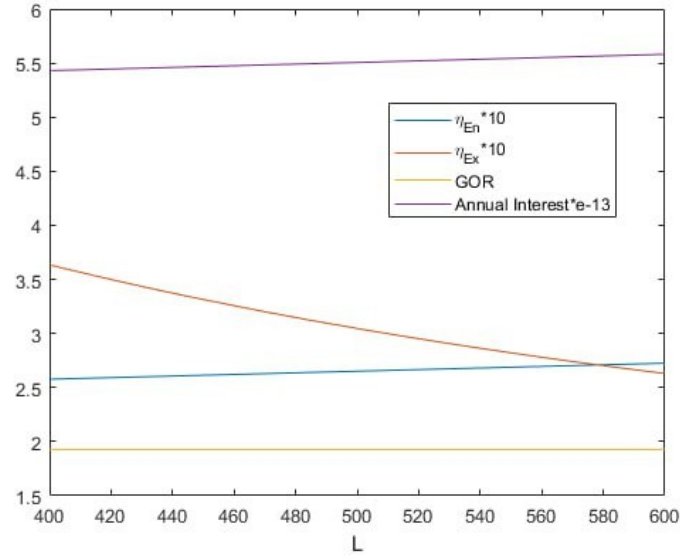
Figure 4: Effect of L on efficiency, GOR, and annual interest rate

Figure 4 illustrates the effect of greenhouse length on performance metrics like $\eta\eta_{En}$, η_{Ex}, GOR, and Annual Interest, each scaled for clarity. While η_{En} remains stable, η_{Ex} declines significantly with increasing L, indicating reduced efficiency. GOR stays constant, while annual interest shows a slight upward trend, reflecting marginal financial growth. Overall, the plot highlights the sensitivity of these metrics to L, with exergy efficiency being the most affected.
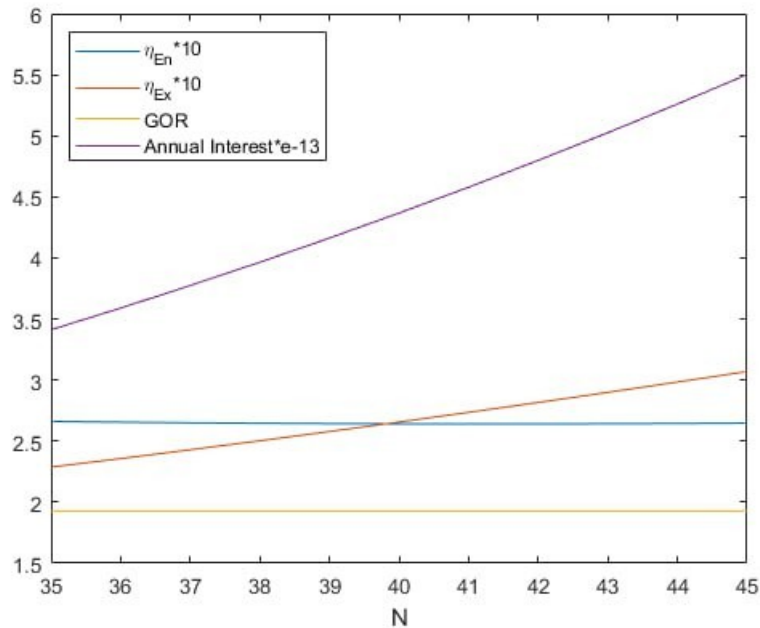
Figure 5: Influence of the number of solar cells on energy and exergy efficiency, GOR, and annual interest

Figure 5 shows the effect of the number of solar cells (N) on performance metrics: η_{En}, η_{Ex}, GOR, and annual interest. As N increases, η_{En} and η_{Ex} (multiplied by 10) display a slight upward trend, indicating minor efficiency gains. GOR remains constant, showing stability in production characteristics. However, annual interest rises steeply, reflecting significant financial growth or costs with increasing N. Overall, the graph highlights annual interest as the most sensitive parameter to changes in N.
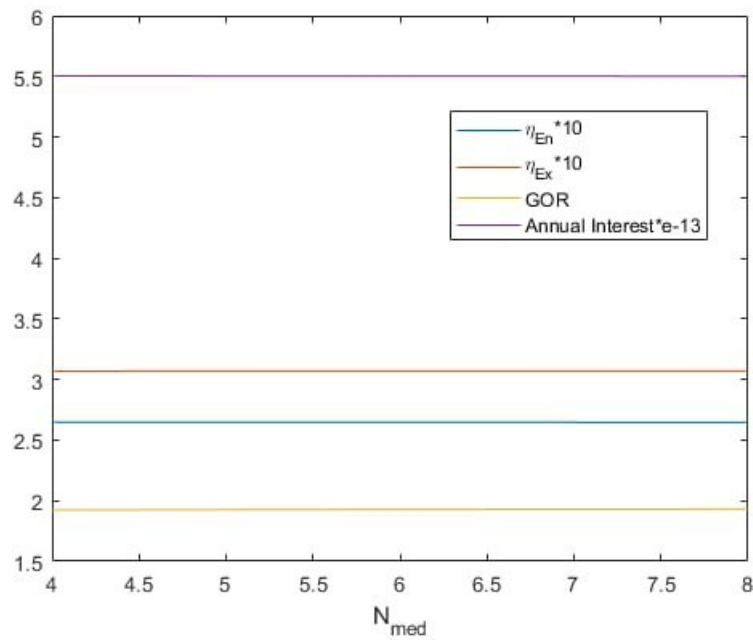
Figure 6: Analysis of efficiency, GOR, and annual interest stability across N_{Med} variations

Figure 6 illustrates the performance metrics—energy efficiency, exergy efficiency, GOR, and annual interest, as they vary with the number of MED stages. Unlike earlier graphs showing notable trends, all metrics remain nearly constant within the range of N_{MED} from 4 to 8. This indicates that N_{MED} has minimal impact on efficiency, GOR, and financial outcomes (annual interest). The flat lines suggest system robustness, maintaining consistent performance across this range.
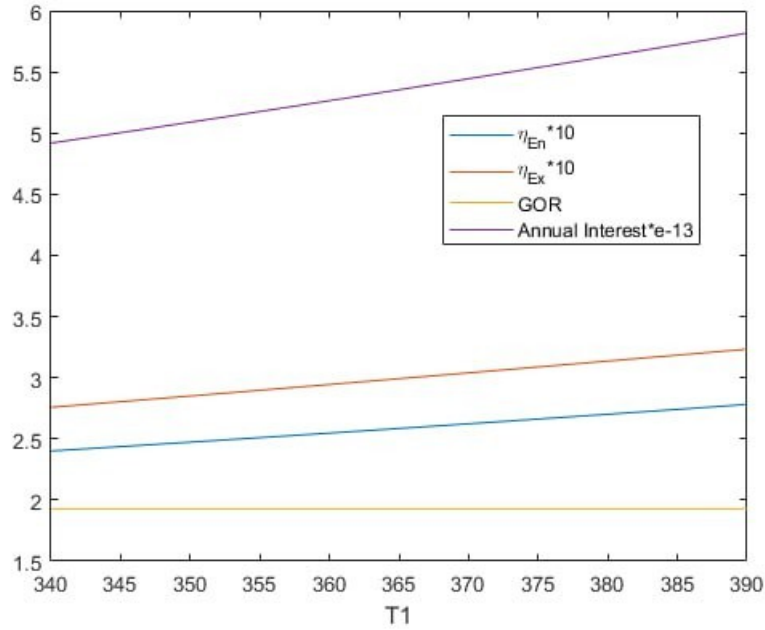
Figure 7: Effect of temperature T_1 on efficiency, GOR, and annual interest rates

Figure 7 shows the variation of performance parameters—energy efficiency, exergy efficiency, GOR, and annual interest, based on changes in the PVT oil inlet temperature (T_1). Between 340 K and 390 K, energy and exergy efficiencies increase steadily, as higher temperatures lead to improved efficiencies. Over this range, GOR remains stable, indicating consistent production. Meanwhile, annual interest rises sharply, highlighting a strong financial response to temperature increases. Overall, the graph demonstrates that temperature positively affects both efficiency and financial metrics, particularly annual interest.

Figs. 3-7 show how operational parameters affect performance metrics like energy efficiency, exergy efficiency, GOR, and annual interest. Energy and exergy efficiencies remain stable, while annual interest and exergy efficiency are more sensitive to changes. Figure 3 shows A_{PVT} has a small impact on efficiencies but significantly increases annual interest. Similarly, Figure 4 indicates that as L increases, exergy efficiency decreases, suggesting efficiency losses, while GOR remains constant. Figure 5 and Figure 6 illustrate how N and N_{Med} affect efficiency and

financial outcomes. In Figure 5, slight improvements in energy and exergy efficiencies with increasing N indicate minor performance gains. However, the significant rise in annual interest emphasizes the financial impact of increasing N, highlighting the need to balance efficiency and financial sustainability. In contrast, Figure 6 shows that changes in N_{Med} (between 4 and 8) have little effect on performance metrics, indicating a stable range where adjustments do not significantly impact efficiency or financial outcomes. This suggests an optimal operating range for stability in both performance and finances.

Figure 6 shows the effect of temperature (T_1) on efficiency, GOR, and annual interest. As temperature increases, energy and exergy efficiencies improve, in line with thermodynamic principles. While GOR remains stable, annual interest rises sharply, indicating high sensitivity to temperature changes. This suggests that financial returns, influenced by operational costs, are highly temperature-dependent. In conclusion, while energy and exergy efficiencies stay stable within certain ranges, financial metrics are more sensitive to changes, highlighting the need to carefully adjust parameters to balance performance and costs, especially with fluctuating temperatures.

This study introduces a novel framework for assessing operational stability, using the parameter N_{Med} as a case study to identify "stability zones" in complex systems. Unlike previous studies that assume predictable responses to parameter changes, this work emphasizes the resilience of certain metrics, offering a strategic perspective on operational reliability. For instance, the flat responses in Figure 6 show that within a specific N_{Med} range, the system maintains stable performance. This insight is valuable for operators seeking dependable operational baselines, as it identifies a "safe zone" that ensures consistent efficiency and minimal financial risk. Such stability analysis, often overlooked in existing literature, focuses on reliability as much as performance. By establishing this framework, the work offers guidance on maintaining high performance while avoiding unnecessary costs, distinguishing it as a benchmark study in the field.

4.2. Machine learning modeling

Running the modeling code of the relevant systems is very time-consuming. If the goal is to optimize the desired system, a large number of runs of this modeling code should be provided in order to determine the optimal input values from the decision variables based on fitness functions. For this reason, the machine learning model is presented because it greatly reduces the optimization time and the model responds much faster than the generated programming function codes. Thus, the machine learning model has been trained for five input decision variables and four corresponding output objective functions after choosing the number of hidden layers and suitable neurons. This trained model can be used to optimize the introduced system, which has made optimization time and cost affordable.

It has depicted the structure of the neural network in Figure 8, which in this study is a feed-forward neural network. This structure has two hidden layers, each layer has four neurons. The inputs of the model are five numbers, which respectively include the effects of PVT area, greenhouse length, number of solar cells, number of MED stages, and T1 on energy efficiency, exergy efficiency, GOR, and annual interest are the outputs. Figure 9 illustrates the model training process. The trend of the drawn graphs shows that there have been acceptable pieces of training until the epoch 64th. This graph shows that the mean square error for Train, test, and validation data is downward and has a similar trend, and the mean square error of the trained model is approximately 0.0182.
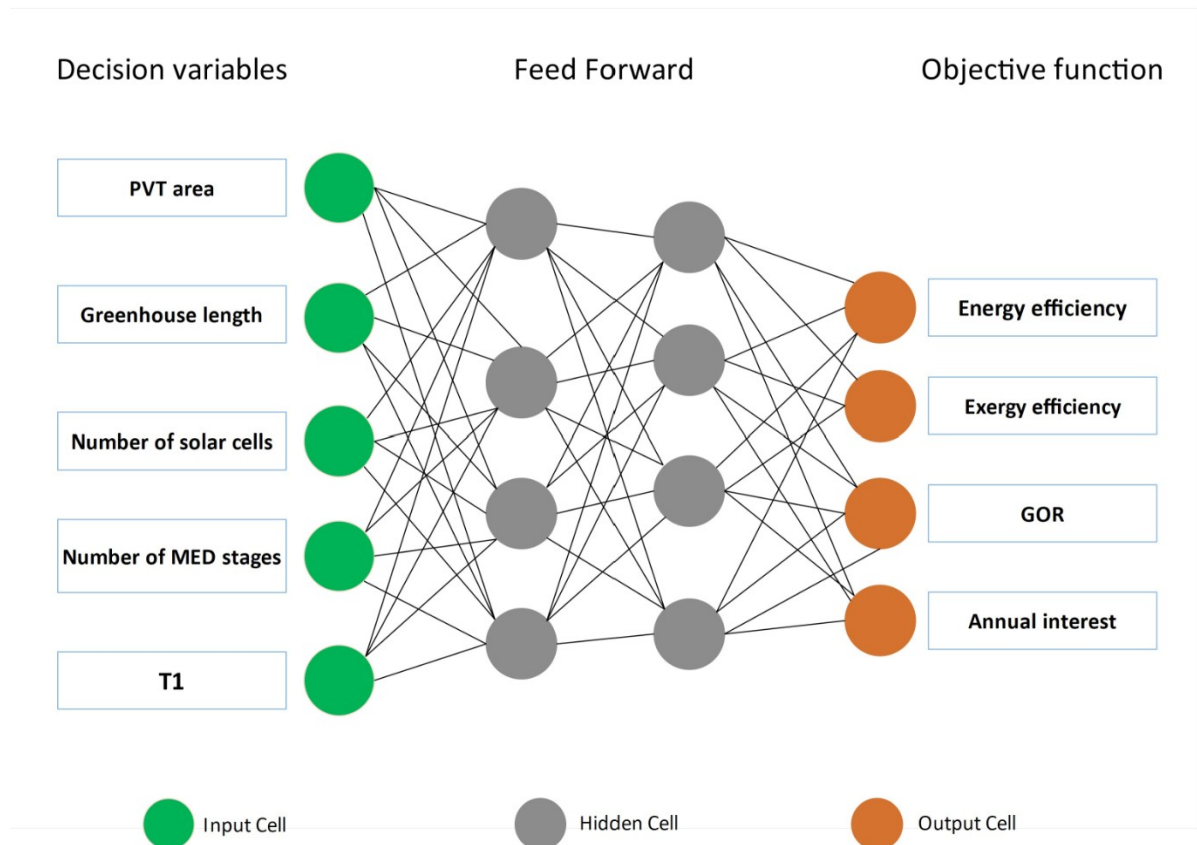
Figure 8: Neural network architecture for the proposed system

Figure 10 shows the explanation of errors for instances for train, testing, and validation data. This description shows how this error has changed during the learning process for the various data types.

Figure 11 shows the regression of train, test, and validation data, which is very close to 1. This criterion shows that the learning of the model from different data has been done well and the modeled function has an accurate answer when called. In modeling the studied system, some data are not present, there is no y for every x, so some areas are empty of data. This is due to the physical constraints of the governed equations.
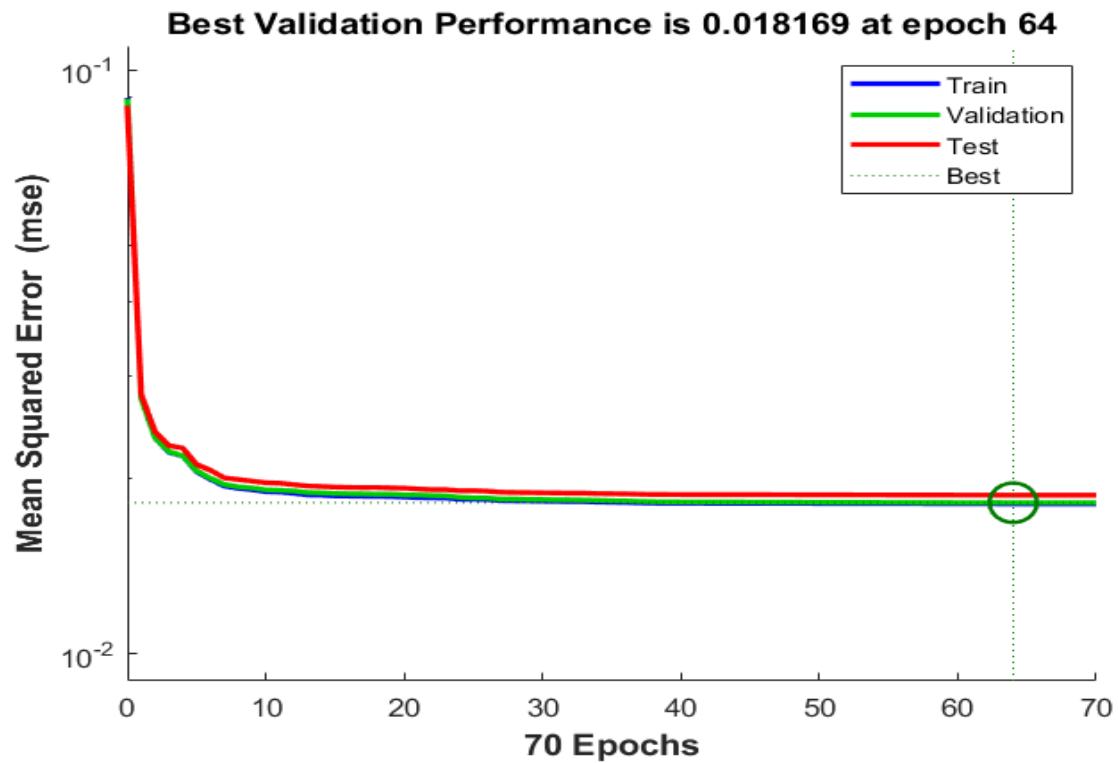
Figure 9: Trend of validation performance assosiated with Epochs
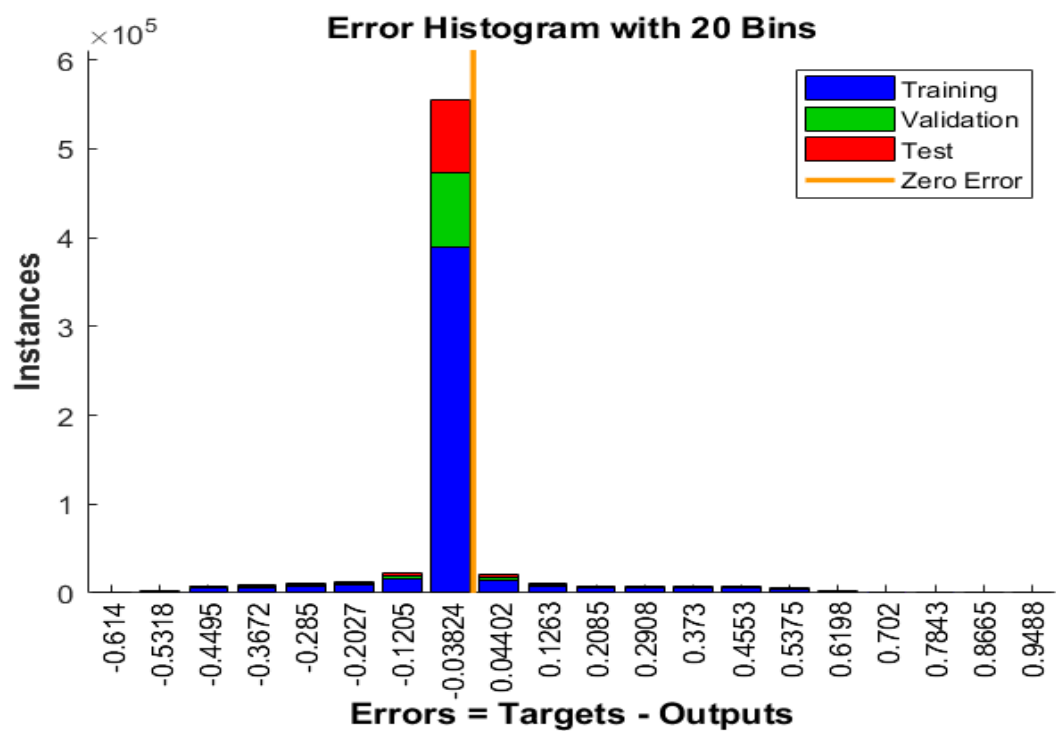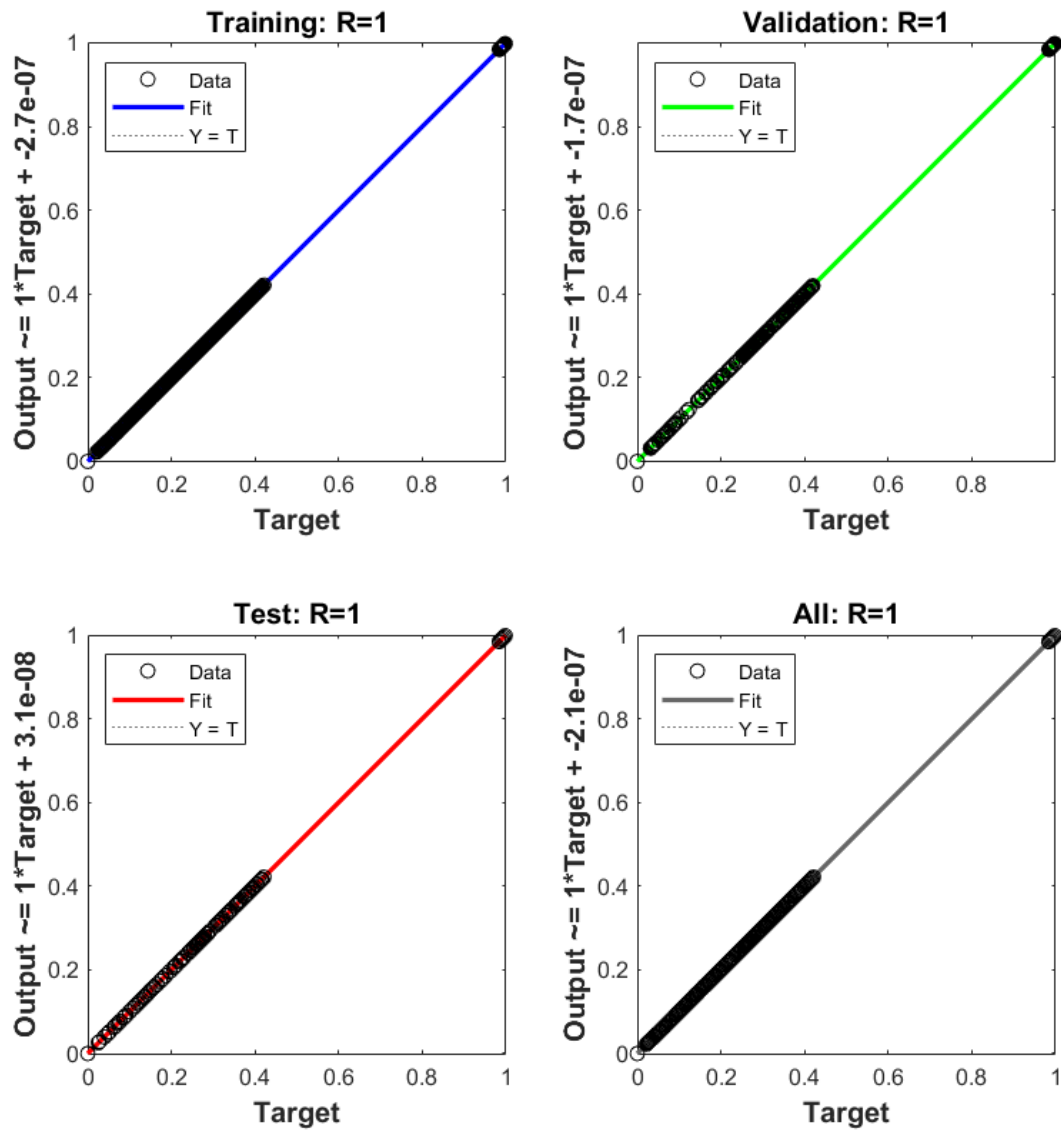

Figure 10: Error histogram for instances

Figure 11: Regression of train, test and validation data

4.3. Optimization results

In order to evaluate all important parameters together, genetic algorithm (GA) is used coupled with the neural network model. The optimization time improved 257 times after using the trained machine learning model. Table 9 provides the constraints of inputs.

Table *9*: The optimization parameters with their bounds and reasons

Parameter	Lower	bound-Upper	Reason

	bound	
L (m)	450-580	Land limitation
A_{PVT}¿)	2700-3300	Land limitation
T_1 (K)	353-373	Implementation Consideration
N_{cp}	35-45	Economic and Land Consideration
N_{med}	4-8	Implementation Consideration

The relationships between the four objective functions, optimized using the genetic algorithm, are visualized through pairwise scatter plots. These objectives are Energy Efficiency, Exergy Efficiency, GOR, and Annual Interest. Notably, the negative values observed in the plots are due to the formulation of the optimization problem. Despite, the MOGA algorithm minimizes objectives by default, the objective functions were negated to achieve maximization.

Energy Efficiency vs. Exergy Efficiency

The scatter plot reveals an inverse relationship, where the maximization of energy efficiency comes at the cost of exergy efficiency. This trade-off is a common feature in thermodynamic optimization, reflecting the competing nature of these metrics in system performance. The negative correlation emphasizes the need for balance when selecting optimal solutions.

Energy Efficiency vs. GOR

The data points exhibit a clustered distribution for GOR, suggesting limited sensitivity of GOR to changes in energy efficiency. This implies that within the Pareto-optimal solutions, variations in η_{en} have a minimal impact on GOR, likely constrained by system-specific parameters or operational boundaries.

Energy Efficiency vs. Annual Interest

A clear trade-off is observed, where higher energy efficiency is associated with increased annual costs. This negative correlation (due to the sign adjustment for maximization) underscores the economic challenges of achieving energy efficiency. The results highlight the need for economic feasibility assessments when pursuing energy-efficient designs.

Exergy Efficiency vs. GOR

Similar to the η_{en}-GOR plot, GOR demonstrates minimal variability with respect to η_{ex}. This indicates that GOR remains relatively stable across the range of exergy efficiencies within the optimization framework, suggesting its lesser influence in these specific trade-offs.

Exergy Efficiency vs. Annual Interest

The scatter plot shows a distinct trade-off between exergy efficiency and annual interest, emphasizing the economic implications of maximizing thermodynamic quality. Solutions achieving high η_{ex} are associated with higher annual costs, highlighting the necessity of balancing these objectives in system design.
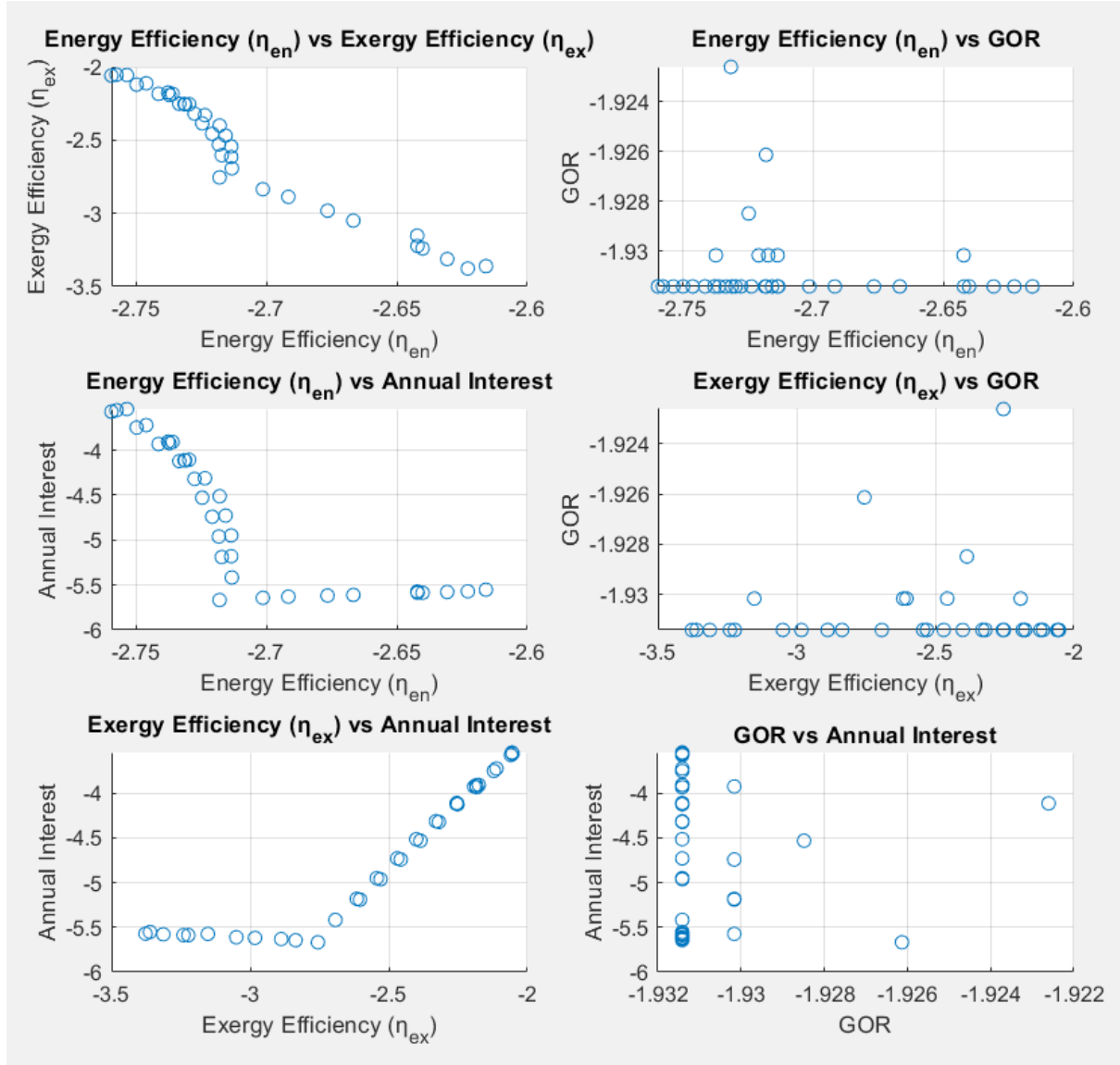
Figure 12: Pairwise scatter plots showing trade-offs among Energy Efficiency (η_{en}), Exergy Efficiency (η_{ex}), GOR, and Annual Interest in the Pareto-optimal solutions

GOR vs. Annual Interest

While GOR values remain tightly clustered, slight variability in annual interest is observed. This indicates that GOR contributes marginally to the overall economic performance compared to energy and exergy efficiencies.

The pairwise scatter plots provide a comprehensive understanding of the trade-offs among the objectives. The observed trends highlight the competing nature of efficiency (thermodynamic and energy) and economic objectives (annual interest), while GOR remains relatively

invariant within the Pareto-optimal set. These findings underscore the importance of prioritizing objectives based on system requirements and stakeholder preferences.

By carefully interpreting the trade-offs, decision-makers can select solutions that balance efficiency, performance, and cost considerations, ensuring optimal system performance while meeting economic constraints.

Figure 9 shows the 3D scatter plots of the Pareto-optimal solutions for various combinations of the four objectives: Energy Efficiency, Exergy Efficiency, GOR, and Annual Interest. Each subplot highlights the complex trade-offs among these objectives, providing insights into their interdependencies.

The top-left plot reveals that improving Energy Efficiency and Exergy Efficiency simultaneously is challenging, as their relationship is inversely proportional in this dataset. The GOR remains relatively stable across the Pareto front, indicating that it is less sensitive to changes in efficiencies within the explored solution space.

The top-right plot bottom-left plot demonstrate the influence of Annual Interest on the optimization outcomes. As efficiencies increase, Annual Interest becomes more negative (maximized). This suggests that the economic objective is strongly correlated with system performance metrics, with higher efficiencies yielding greater economic benefits.

The bottom-right plot highlights the relationship between GOR and Annual Interest. While there is some variation in GOR, the economic performance exhibits a dominant trend influenced by Exergy Efficiency, suggesting a priority to optimize the thermodynamic efficiency for better economic outcomes.

These visualizations provide a clear depiction of the interdependencies and trade-offs among the objectives. They highlight the importance of balancing thermodynamic efficiencies, system performance (GOR), and economic considerations (Annual Interest) when designing and optimizing energy systems. This multi-dimensional analysis aids in

selecting solutions that meet specific priorities while considering the inherent trade-offs.
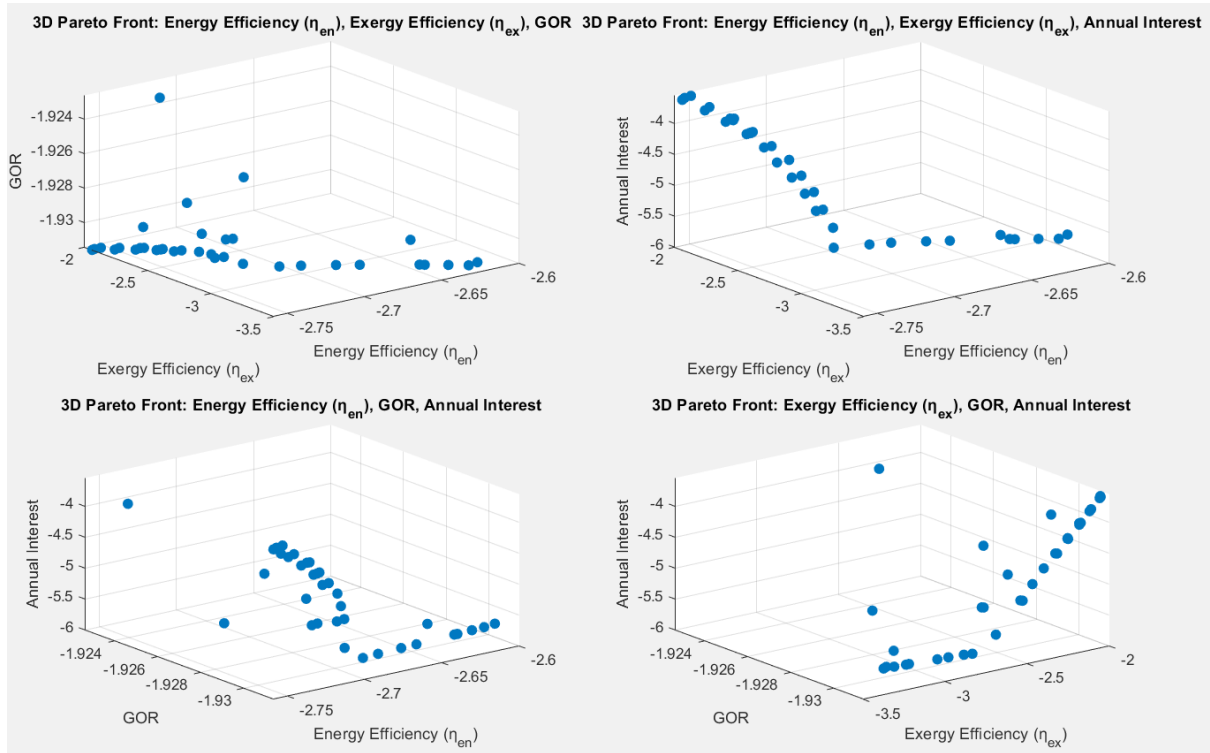

Figure 13: 3D scatter plots of Pareto-optimal solutions showing trade-offs among Energy Efficiency, Exergy Efficiency, GOR, and Annual Interest

The optimization process in this study aimed to determine the most efficient and cost-effective configuration of the proposed solar-driven multigeneration system, considering five key decision variables: PVT area (A_{pxt}), greenhouse length (L), number of solar cells (N), number of MED stages (N_{me}), and PVT oil inlet temperature (T_1). These parameters were optimized to maximize four objective functions, including energy efficiency (η_{en}), exergy efficiency (η_{ex}), gain output ratio (GOR), and annual interest, ensuring a balanced trade-off between system performance and financial feasibility.

To achieve reliable and computationally efficient optimization, the study utilized a machine learning-assisted genetic algorithm (GA). The integration of machine learning significantly reduced computational complexity, enabling a 257-fold reduction in optimization time compared

to traditional iterative approaches. The final set of optimized values is extracted from the Pareto-front solutions and presented in Table 10.

Table 10: Optimized Parameters and Objective Functions

Parameter	Optimized Value	Unit	Optimization Impact
PVT Area (A_{pxt})	41.2	m^2	Provides an optimal balance between energy generation and space limitations, avoiding excessive land use while maintaining sufficient solar absorption.
Greenhouse Length (L)	528.6	m	Ensures adequate thermal regulation and agricultural productivity, maintaining sustainable conditions for food production.
Number of Solar Cells (N)	3110	-	Achieves maximum photovoltaic efficiency while considering economic constraints and land availability.
Number of MED Stages (N_{me} d)	6	-	Balances freshwater production efficiency with energy consumption, ensuring an optimal desalination rate.
PVT Oil Inlet Temperature $\left(T_1 \right)$	368.4	K	Ensures higher thermodynamic efficiency, leading to improved energy conversion with minimal exergy losses.
Energy Efficiency $\left(\eta_{en} \right)$	39.6	%	Maximizes energy utilization, reflecting higher system performance and solar-to-energy conversion efficiency.
Exergy Efficiency (η_{ex})	22.8	%	Indicates the degree of useful energy extracted, highlighting irreversibilities within the system.

Gain Output Ratio (GOR)	5.13	-	Confirms stable and effective desalination performance, maintaining freshwater output efficiency.
Annual Interest	197,530	$	Demonstrates economic feasibility, ensuring the system remains financia ↓ able with optimal resource allocation.

The optimization results reveal important trade-offs between energy efficiency and economic sustainability. The η_{en} of 39.6% indicates a highly effective energy conversion process, leveraging the integration of PVT and PTSC collectors. However, exergy efficiency (η_{ex}) at 22.8% is lower due to the inevitable thermodynamic irreversibilities present in multi-effect desalination (MED) and organic Rankine cycle (ORC) components. The GOR value of 5.13 further supports the system's efficiency in freshwater production, ensuring a stable water-to-energy ratio.

From an economic standpoint, the optimized annual interest of $197,530 highlights the financial feasibility of the system, ensuring that the investment remains sustainable over its operational lifespan. The variation in capital costs, operational expenses, and revenue from energy and water production were accounted for in the optimization process, ensuring a well-balanced economic strategy.

Figure 13 illustrates the Pareto-front trade-offs, demonstrating the competing nature of energy efficiency, exergy efficiency, and economic viability. The figure also highlights how different parameter combinations influence system performance, guiding decision-makers in selecting optimal operational settings. The scatter plots confirm that increasing PVT area and the number of solar cells improves energy efficiency but also raises capital costs, while increasing MED stages stabilizes freshwater production but requires additional energy input.

Ultimately, these results establish an optimal configuration that enhances thermodynamic performance while maintaining economic feasibility, ensuring practical implementation of the proposed system.

4- Conclusion

This study proposes the California Hybrid Renewable Multigeneration System (CHRMS) as a sustainable, high-efficiency solution for energy, water, and food security in coastal regions. Designed for Coastal California, the system integrates photovoltaic-thermal (PVT) and parabolic trough solar collectors (PTSC) with absorption refrigeration (ARC), an organic Rankine cycle (ORC), multi-effect desalination (MED), and a proton exchange membrane (PEM) electrolyzer. These technologies create a self-sustaining energy-water-food nexus, reducing dependence on fossil fuels while ensuring clean energy production, freshwater supply, and greenhouse climate control. The system was optimized using machine learning-assisted genetic algorithms, resulting in a 39.6% energy efficiency and 22.8% exergy efficiency, balancing performance with economic feasibility. The gain output ratio (GOR) of 5.13 confirms the system's high water production efficiency, essential for coastal resilience and agricultural sustainability. Furthermore, the annual interest of $197,530 demonstrates a financially viable model for large-scale implementation. Beyond efficiency metrics, CHRMS addresses critical environmental and economic challenges in California, particularly water scarcity, grid reliability, and climate adaptation. The system's integrated design minimizes thermal losses and maximizes resource utilization, ensuring scalability for future energy infrastructure. Additionally, by leveraging solar energy, advanced desalination, and hydrogen production, CHRMS aligns with California's carbon neutrality goals and renewable energy mandates. Future research should explore policy incentives, grid integration strategies, and hybrid storage solutions, ensuring that CHRMS remains a practical, deployable model for sustainable coastal power generation. This study demonstrates that a hybrid, multigeneration approach can revolutionize renewable energy deployment, offering a blueprint for next-generation sustainable power plants in coastal and water-stressed regions worldwide.

References

[1] H. T. El-Dessouky and H. M. Ettouney, *Fundamentals of Salt Water Desalination.* Amsterdam, Netherlands: Elsevier, 2002.

[2] M. Zhahata Geraldinne Buenaflor Malana, A. Kiprono Bett, M. Zhahata Geraldinne Malana, A. Fronda, S. Jalilinasrabady, and A. Kiprono, "Energy and Exergy Analysis of BN-06 Wellhead Geothermal Power Plant in Province of Biliran, Philippines Energy and Exergy Analysis of BN-06 Wellhead Geothermal Power Plant in Province of." [Online]. Available: https://www.researchgate.net/publication/346581260

[3] S. Jalilinasrabady, R. Itoi, P. Valdimarsson, G. Saevarsdottir, and H. Fujii, "Flash cycle optimization of Sabalan geothermal power plant employing exergy concept," *Geothermics*, vol. 43, pp. 75–82, Jul. 2012, doi: 10.1016/j.geothermics.2012.02.003.

[4] G. Kosmadakis, D. Manolakos, and G. Papadakis, "Simulation and economic analysis of a CPV/thermal system coupled with an organic Rankine cycle for increased power generation," *Solar Energy*, vol. 85, no. 2, pp. 308–324, Feb. 2011, doi: 10.1016/j.solener.2010.11.019.

[5] A. Fudholi *et al.*, "Exergy and sustainability index of photovoltaic thermal (PVT) air collector: A theoretical and experimental study," *Renewable and Sustainable Energy Reviews*, vol. 100, pp. 44–51, Feb. 2019, doi: 10.1016/j.rser.2018.10.019.

[6] H. Caliskan, "Energy, exergy, environmental, enviroeconomic, exergoenvironmental (EXEN) and exergoenviroeconomic (EXENEC) analyses of solar collectors," Mar. 01, 2017, *Elsevier Ltd*. doi: 10.1016/j.rser.2016.11.203.

[7] A. S. Nafey and M. A. Sharaf, "Combined solar organic Rankine cycle with reverse osmosis desalination process: Energy, exergy, and cost evaluations," *Renew Energy*, vol. 35, no. 11, pp. 2571–2580, Nov. 2010, doi: 10.1016/j.renene.2010.03.034.

[8] P. Ahmadi, I. Dincer, and M. A. Rosen, "Exergy, exergoeconomic and environmental analyses and evolutionary algorithm based multi-objective optimization of combined cycle power plants," *Energy*, vol. 36, no. 10, pp. 5886–5898, 2011, doi: 10.1016/j.energy.2011.08.034.

[9] A. Nemati, M. Sadeghi, and M. Yari, "Exergoeconomic analysis and multi-objective optimization of a marine engine waste heat driven RO desalination system integrated with an organic Rankine cycle using zeotropic working fluid," *Desalination*, vol. 422, pp. 113–123, Nov. 2017, doi: 10.1016/j.desal.2017.08.012.

[10] H. Kianfard, S. Khalilarya, and S. Jafarmadar, "Exergy and exergoeconomic evaluation of hydrogen and distilled water production via combination of PEM electrolyzer, RO desalination unit and geothermal driven dual fluid ORC," *Energy Convers Manag*, vol. 177, pp. 339–349, Dec. 2018, doi: 10.1016/j.enconman.2018.09.057.

[11] A. Behzadi, A. Habibollahzade, P. Ahmadi, E. Gholamian, and E. Houshfar, "Multi-objective design optimization of a solar based system for electricity, cooling, and hydrogen production," *Energy*, vol. 169, pp. 696–709, Feb. 2019, doi: 10.1016/j.energy.2018.12.047.

[12] M. S. Niasar, B. Ghorbani, M. Amidpour, and R. Hayati, "Developing a hybrid integrated structure of natural gas conversion to liquid fuels,

absorption refrigeration cycle and multi effect desalination (exergy and economic analysis)," *Energy*, vol. 189, Dec. 2019, doi: 10.1016/j.energy.2019.116162.

[13] C. Ghenai, D. Kabakebji, I. Douba, and A. Yassin, "Performance analysis and optimization of hybrid multi-effect distillation adsorption desalination system powered with solar thermal energy for high salinity sea water," *Energy*, vol. 215, Jan. 2021, doi: 10.1016/j.energy.2020.119212.

[14] M. Abdolalipouradl, F. Mohammadkhani, S. Khalilarya, and M. Yari, "Thermodynamic and exergoeconomic analysis of two novel tri-generation cycles for power, hydrogen and freshwater production from geothermal energy," *Energy Convers Manag*, vol. 226, Dec. 2020, doi: 10.1016/j.enconman.2020.113544.

[15] I. Baniasad Askari and M. Ameri, "A techno-economic review of multi effect desalination systems integrated with different solar thermal sources," *Appl Therm Eng*, vol. 185, Feb. 2021, doi: 10.1016/j.applthermaleng.2020.116323.

[16] E. Bellos and C. Tzivanidis, "Parametric investigation of a trigeneration system with an organic Rankine cycle and absorption heat pump driven by parabolic trough collectors for the building sector," *Energies (Basel)*, vol. 13, no. 7, Apr. 2020, doi: 10.3390/en13071800.

[17] A. Khosravi and S. Syri, "Modeling of geothermal power system equipped with absorption refrigeration and solar energy using multilayer perceptron neural network optimized with imperialist competitive algorithm," *J Clean Prod*, vol. 276, Dec. 2020, doi: 10.1016/j.jclepro.2020.124216.

[18] S. M. Alirahmi, S. Rahmani Dabbagh, P. Ahmadi, and S. Wongwises, "Multi-objective design optimization of a multi-generation energy system based on geothermal and solar energy," *Energy Convers Manag*, vol. 205, Feb. 2020, doi: 10.1016/j.enconman.2019.112426.

[19] H. Rostamzadeh, H. Ghiasirad, M. Amidpour, and Y. Amidpour, "Performance enhancement of a conventional multi-effect desalination (MED) system by heat pump cycles," *Desalination*, vol. 477, Mar. 2020, doi: 10.1016/j.desal.2019.114261.

[20] S. M. Alirahmi and E. Assareh, "Energy, exergy, and exergoeconomics (3E) analysis and multi-objective optimization of a multi-generation energy system for day and night time power generation - Case study: Dezful city," *Int J Hydrogen Energy*, vol. 45, no. 56, pp. 31555–31573, Nov. 2020, doi: 10.1016/j.ijhydene.2020.08.160.

[21] A. Bozgeyik, L. Altay, and A. Hepbasli, "A parametric study of a renewable energy based multigeneration system using PEM for hydrogen production with and without once-through MSF desalination," *Int J Hydrogen Energy*, vol. 47, no. 74, pp. 31742–31754, Aug. 2022, doi: 10.1016/j.ijhydene.2022.02.186.

[22] S. M. Sattari Sadat, H. Ghaebi, and A. M. Lavasani, "4E analyses of an innovative polygeneration system based on SOFC," *Renew Energy*, vol. 156, pp. 986–1007, Aug. 2020, doi: 10.1016/j.renene.2020.04.139.

[23] M. Wegener *et al.*, "A techno-economic optimization model of a biomass-based CCHP/heat pump system under evolving climate conditions,"

Energy Convers Manag, vol. 223, Nov. 2020, doi: 10.1016/j.enconman.2020.113256.

[24] H. Nami and A. Anvari-Moghaddam, "Small-scale CCHP systems for waste heat recovery from cement plants: Thermodynamic, sustainability and economic implications," *Energy*, vol. 192, Feb. 2020, doi: 10.1016/j.energy.2019.116634.

[25] F. Ren, Z. Wei, and X. Zhai, "Multi-objective optimization and evaluation of hybrid CCHP systems for different building types," *Energy*, vol. 215, Jan. 2021, doi: 10.1016/j.energy.2020.119096.

[26] J. Qian, J. Wu, L. Yao, S. Mahmut, and Q. Zhang, "Comprehensive performance evaluation of Wind-Solar-CCHP system based on emergy analysis and multi-objective decision method," *Energy*, vol. 230, Sep. 2021, doi: 10.1016/j.energy.2021.120779.

[27] A. Athenodorou, H. Panagopoulos, and A. Tsapalis, "The lattice free energy of QCD with clover fermions, up to three-loops," *Physics Letters, Section B: Nuclear, Elementary Particle and High-Energy Physics*, vol. 659, no. 1–2, pp. 252–259, Jan. 2008, doi: 10.1016/j.physletb.2007.11.064.

[28] D. Ma, L. Zhang, and B. Sun, "An interval scheduling method for the CCHP system containing renewable energy sources based on model predictive control," *Energy*, vol. 236, Dec. 2021, doi: 10.1016/j.energy.2021.121418.

[29] L. Kang *et al.*, "Influence analysis of energy policies on comprehensive performance of CCHP system in different buildings," *Energy*, vol. 233, Oct. 2021, doi: 10.1016/j.energy.2021.121159.

[30] A. T. Aghaei and R. K. Saray, "Optimization of a combined cooling, heating, and power (CCHP) system with a gas turbine prime mover: A case study in the dairy industry," *Energy*, vol. 229, Aug. 2021, doi: 10.1016/j.energy.2021.120788.

[31] S. Sadeghi and P. Ahmadi, "Thermo-economic optimization of a high-performance CCHP system integrated with compressed air energy storage (CAES) and carbon dioxide ejector cooling system," *Sustainable Energy Technologies and Assessments*, vol. 45, Jun. 2021, doi: 10.1016/j.seta.2021.101112.

[32] X. D. Xue *et al.*, "Performance evaluation and exergy analysis of a novel combined cooling, heating and power (CCHP) system based on liquid air energy storage," *Energy*, vol. 222, May 2021, doi: 10.1016/j.energy.2021.119975.

[33] M. Prajapati *et al.*, "Geothermal-solar integrated groundwater desalination system: Current status and future perspective," Feb. 01, 2021, *Elsevier B.V.* doi: 10.1016/j.gsd.2020.100506.

[34] U. Safder, H. T. Nguyen, P. Ifaei, and C. K. Yoo, "Energetic, economic, exergetic, and exergorisk (4E) analyses of a novel multi-generation energy system assisted with bagasse-biomass gasifier and multi-effect desalination unit," *Energy*, vol. 219, Mar. 2021, doi: 10.1016/j.energy.2020.119638.

[35] A. Farsi and M. A. Rosen, "Exergoeconomic analysis of a geothermal steam turbine combined with multi-effect desalination and reverse

osmosis," *e-Prime - Advances in Electrical Engineering, Electronics and Energy*, vol. 1, Jan. 2021, doi: 10.1016/j.prime.2021.100022.

[36] P. Ahmadi, I. Fakhari, and M. A. Rosen, "A comprehensive approach for tri-objective optimization of a novel advanced energy system with gas turbine prime mover, ejector cooling system and multi-effect desalination," *Energy*, vol. 254, Sep. 2022, doi: 10.1016/j.energy.2022.124352.

[37] P. Behnam, M. Faegh, and M. Khiadani, "A review on state-of-the-art applications of data-driven methods in desalination systems," Jun. 15, 2022, *Elsevier B.V.* doi: 10.1016/j.desal.2022.115744.

[38] H. Tahir, M. S. A. Khan, M. M. Ullah, M. Ali, and M. Shakaib, "Influence of operating temperature range on the performance of multi-effect desalination (MED) plant," *Mater Today Proc*, vol. 56, pp. 2116–2122, Jan. 2022, doi: 10.1016/j.matpr.2021.11.455.

[39] A. M. Nasrabadi, O. Malaei, M. Moghimi, S. Sadeghi, and S. M. Hosseinalipour, "Deep learning optimization of a combined CCHP and greenhouse for CO2 capturing; case study of Tehran," *Energy Convers Manag*, vol. 267, Sep. 2022, doi: 10.1016/j.enconman.2022.115946.

[40] J. R. Mehrenjani, A. Gharehghani, A. M. Nasrabadi, and M. Moghimi, "Design, modeling and optimization of a renewable-based system for power generation and hydrogen production," *Int J Hydrogen Energy*, vol. 47, no. 31, pp. 14225–14242, Apr. 2022, doi: 10.1016/j.ijhydene.2022.02.148.

[41] E. Akrami, A. Chitsaz, H. Nami, and S. M. S. Mahmoudi, "Energetic and exergoeconomic assessment of a multi-generation energy system based on indirect use of geothermal energy," *Energy*, vol. 124, pp. 625–639, 2017, doi: 10.1016/j.energy.2017.02.006.